Construction of BiOBr/BNQDs Heterostructure Photocatalyst and Performance Studies of Photocatalytic Degradation of RhB

Yufeng Qin , Xinyu Peng , Tong Wu , Yi Zhong , Hong Xu , Zhiping Mao * , Linping Zhang *

Posted Date: 23 July 2025

doi: 10.20944/preprints202507.1891.v1

Keywords: BiOBr; photocatalysis; heterojunction; BNQDs; dye degradation; Rhodamine B (RhB)

 doi:10.20944/preprints202507.1891.v1

Article

Construction of BiOBr/BNQDs Heterostructure Photocatalyst and Performance Studies of Photocatalytic Degradation of RhB

Yufeng Qin, Xinyu Peng, Tong Wu, Yi Zhong, Hong Xu, Zhiping Mao * and Linping Zhang *

Key Lab of Science and Technology of Eco-textile, College of Chemistry and Chemical Engineering, Donghua University, Shanghai 201620, China

* Correspondence: zhang_lp@dhu.edu.cn

Abstract

As a common semiconductor material, BiOBr has a unique layered structure and a suitable bandgap. However, the slow electron-hole separation efficiency leads to poor photocatalytic performance. To solve this problem, BiOBr/BNQDs heterojunctions were constructed. BiOBr/BNQDs composite photocatalysts were prepared by the solvothermal method, and the cocatalyst BNQDs were loaded onto BiOBr via electrostatic adsorption to enhance the photocatalytic degradation activity towards Rhodamine B (RhB). The photocatalysts were characterized by FT-IR, XRD, XPS, SEM-EDS, UV-Vis, PL, EIS, etc. Compared with pure BiOBr, the construction of heterojunctions BiOBr/BNQDs realized the rapid elimination of weak carriers and the effective separation and enrichment of high-energy carriers, which improved the efficiency of photocatalytic degradation of RhB. Among them, BiOBr/BNQDs-8.3% demonstrated the highest photocatalytic activity. The degradation rate of RhB under visible light irradiation for 60 min was up to 98.56%, and the reaction rate constant was 0.0696 min^{-1}, which was 2.80 times of pure BiOBr. Moreover, after five photocatalytic cycles, the degradation rate was still 87.58%, demonstrating good cycling stability.

Keywords: BiOBr; photocatalysis; heterojunction; BNQDs; dye degradation; Rhodamine B (RhB)

1. Introduction

The rapid advancement of industrialization has driven significant economic growth [1], but it also resulted in a substantial increase in industrial wastewater [2]. Among various pollutants in wastewater, Rhodamine B (RhB) is of particular concern due to its widespread use in textile dyeing, leather processing, and fluorescent labeling, attributed to its excellent solubility and photostability [3]. However, its extensive use has deleterious effects on human health and pollutes soil and water sources, posing a serious threat to human health and ecological safety [4]. At present, the predominant wastewater treatment methodologies encompass physical adsorption and biofilm separation. A comparison of conventional treatment methods with the photocatalytic degradation of RhB using bismuth-based semiconductor materials reveals significant advantages, including environmental sustainability, non-toxicity, and a high degree of efficiency and cost-effectiveness [5].

Bismuth bromide oxide (BiOBr) has gained notable popularity due to its distinctive structure of alternating stacks of $[Bi_2O_2]^{2+}$layers and double Br^- layers. Its applications include the mitigation of CO_2 emissions and the photocatalytic degradation of organic pollutants [6]. Nevertheless, pristine BiOBr suffers from intrinsic limitations, including a low density of active sites and rapid recombination of photogenerated electron–hole pairs, which severely restrict its photocatalytic efficiency [7]. The predominant contemporary approaches to address these issues include loading co-catalysts [8], defect engineering [9], heterostructure construction [10–12], and element doping [13]. For instance, Liu et al. reported loading NH_2–UiO-66 onto prepared BiOBr nanosheets for CO_2 reduction to produce CO. The resulting heterostructure photocatalytic system exhibits enhanced light

 doi:10.20944/preprints202507.1891.v1

responsiveness, a larger specific surface area, and faster electron-hole pair separation performance [14].

In recent years, quantum dots (QDs) have been widely used in the field of photocatalysis due to their unique quantum confinement effect, a large number of edge active sites, and the advantages of being green and harmless [15,16]. Such as graphene (GQDs) [17], carbon (CQDs) [18], boron nitride (BNQDs) [19], etc. Among these non-metallic quantum dots, BNQDs form an electronegativity gradient between the boron vacancies at the edges and the nitrogen atoms in the hexagonal lattice, constructing a built-in electric field in the vertical direction. This electric field drives the photogenerated holes to migrate to the surface of the quantum dots, effectively constructing a transport channel for photogenerated holes [20,21].

In this work, BNQDs was combined with BiOBr to promote the rapid separation of electron-hole pairs, enhancing the photocatalytic activity of BiOBr for the degradation of RhB. BiOBr/BNQDs heterostructure was prepared via a facile hydrothermal method. Through concurrent electrochemical tests, radical scavenging experiments and band structure analysis, the synergistic effects of the BiOBr/BNQDs composite material in the photocatalytic degradation process are mechanistically analyzed. It offers a promising strategy for designing efficient and durable visible-light-driven photocatalysts via heterojunction.

2. Results and Discussion

The XRD characterization of the crystal phase and composition of the synthesized catalyst samples was shown in Figure 1a, all the diffraction peaks of BiOBr and BNQDs were observed, indicating the successful synthesis of samples with high crystallinity. Among them, the sharp peaks around 2θ at 10.9 °, 21.9 °, 25.6 °, 31.7 °, and 32.4 ° were attributed to the (001), (002), (101), (102), and (110) crystal planes of BiOBr, respectively, which were consistent with the standard card of BiOBr (PDF#85—0862) [22]. The diffraction peaks at 25.5° and 42° correspond to the (002) and (100) crystal planes of BN, respectively. Compared with pure BiOBr, no obvious diffraction peaks of BNQDs were detected in the BiOBr/BNQDs composite, because only a small amount of BNQDs existed in the composite, and the (002) plane peak of BNQDs coincide with the (101) plane peak of BiOBr. Also it proved that the combination of BNQDs did not significantly change the crystal structure of BiOBr [23]. The chemical structures of the synthesized samples were characterized by FT-IR spectroscopy. As shown in Figure 1b, in the spectrum of pure BiOBr, the peak at 510 cm^{-1} was from the Bi-O stretching and deformation vibrations. In pure BNQDs, the peaks at 1410 cm^{-1} belong to the B-N bond, and the peaks at 1190 cm^{-1} and 3200 cm^{-1} belong to the stretching modes of the B-O bond and O-H bond of B-OH group, respectively. In the BiOBr/BNQDs composite, with the introduction of BNQDs, several important peaks belonging to BNQDs were observed at 1190, 1410 and 3200 cm^{-1}, which belong to the stretching modes of the B-O, B-N, and O-H bond of B-OH group, respectively. Meanwhile, an O-H bending vibration appeared at 3400 cm^{-1}, which may come from water molecules in the air or hydroxyl groups on the sample surface [24]. The results obtained from XRD and FT-IR proved the successful synthesis of BiOBr, BNQDs, and BiOBr/BNQDs.

The morphological characteristics of the catalysts were investigated using scanning electron microscopy (SEM) and transmission electron microscopy (TEM). As demonstrated in Figure 2a, the prepared BiOBr were nanoflower-shaped microspheres assembled from a substantial number of ultra-thin nanosheets, with a diameter of approximately 4-5 μm. This hierarchical structure, characterized by a substantial amount of open, free space, has the potential to provide a larger contact area for the system [25]. As illustrated in Figure 2b, the mean lateral dimension of BNQDs was estimated to be approximately 3 nm. The BNQDs demonstrate remarkable crystallinity, exhibiting well-defined and orderly parallel lattice stripes on the surfaces. The interatomic spacing of 0.21 nm corresponds closely to the (100) crystal plane of BN, suggesting a high degree of structural order [26]. Figure 2c presents the SEM image of the BiOBr/BNQDs-8.3% composite material. The composite maintains the morphology of the nano-flower-like microspheres, suggesting that BiOBr remains stable during the composite process. A thorough analysis of the EDS mapping images in Figure 2d–

 doi:10.20944/preprints202507.1891.v1

h reveals the distribution of Bi, Br, O, B, and N elements. The analysis demonstrates that the B and N elements are uniformly distributed on the surface of BiOBr [27]. These results confirm the successful synthesis of BiOBr/BNQDs.

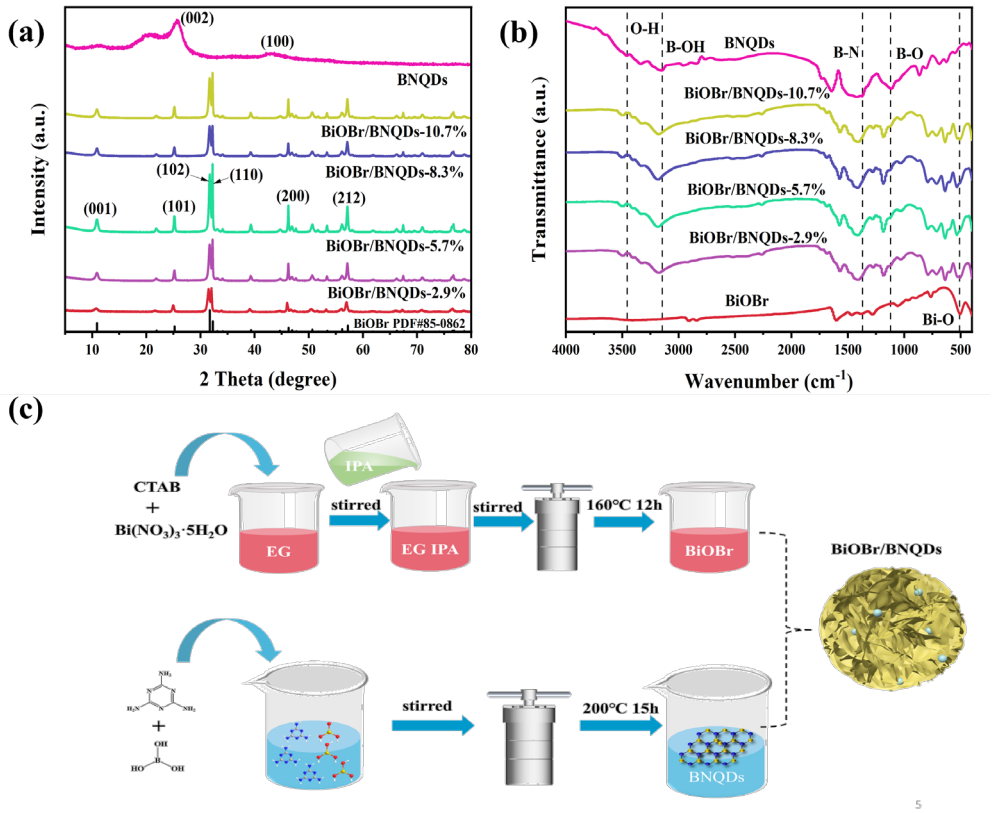

Figure 1. (a) XRD patterns and (b) FT-IR spectra of BiOBr, BNQDs and BiOBr/BNQDs with different mass ratios. (c) Diagrammatic sketch of the synthesis process.

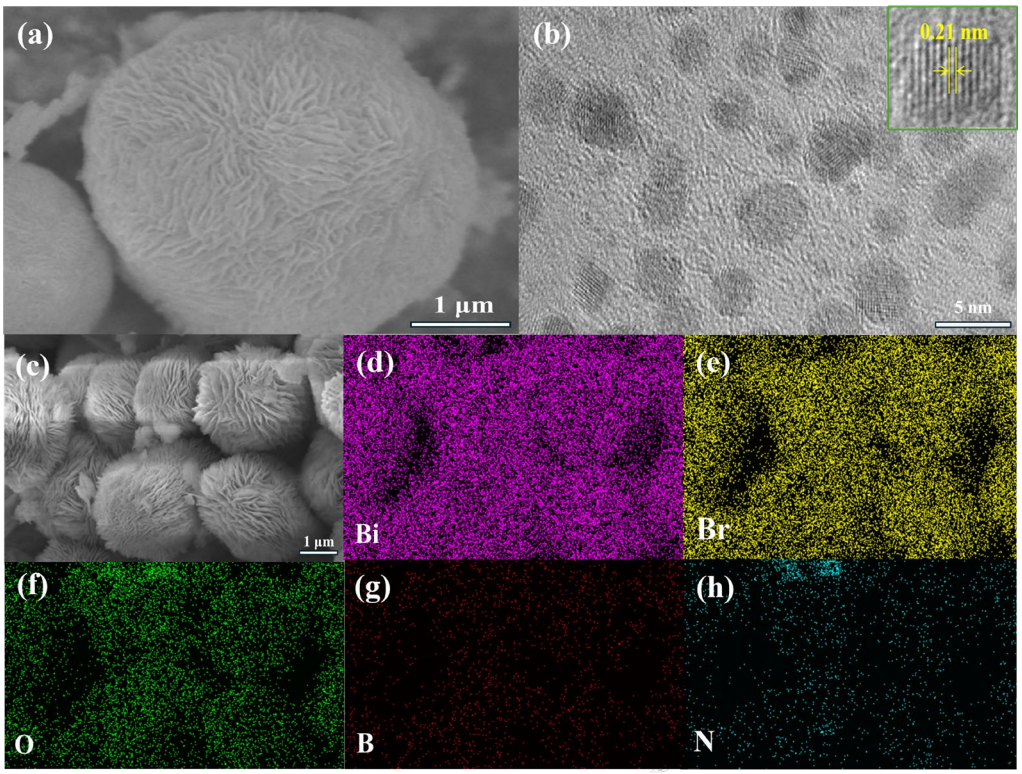

 doi:10.20944/preprints202507.1891.v1

Figure 2. (a) SEM images of BiOBr and (b) TEM images of BNQDs. (c) SEM image of BiOBr/BNQDs-8.3%. EDS mapping images (d) Bi, (e) Br, (f) O, (g) B, and (h) N.

Subsequent analysis of the elemental composition and valence states of the prepared catalysts were conducted using X-ray photoelectron (XPS) testing. As illustrated in Figure 3a, the composition of BiOBr consists of Bi, O, and Br elements, while the BiOBr/BNQDs-8.3% composite material was constituted of Bi, Br, O, B, and N elements. In the high-resolution XPS spectrum of Bi 4f in Figure 3b, for BiOBr, the two peaks at 159.1 and 164.42 eV correspond to the Bi $4f_{7/2}$ peak and Bi $4f_{5/2}$ peak, respectively [28]. In contrast, the Bi 4f peaks in BiOBr/BNQDs-8.3% were identified at 159.03 and 164.3 eV, which implies that in BiOBr and BiOBr/BNQDs-8.3% samples, Bi was mainly present in the form of Bi^{3+}. As illustrated in Figure 3c, the Br 3d XPS spectrum of pure BiOBr exhibits two peaks at 68.32 and 69.3 eV, which were attributed to the characteristic peaks of Br $3d_{5/2}$ and Br $3d_{3/2}$, respectively. From Figure 3d, the O 1s spectra of the original BiOBr could be separated into two peaks at 530.03 and 531.28 eV, while BiOBr/BNQDs-8.3% could be decomposed into three peaks at 529.81, 531.02, and 533.33 eV, corresponding to lattice oxygen (Bi-O) in BiOBr, oxygen vacancies (OVs) formed during synthesis, and chemically adsorbed oxygen species (-OH), respectively [29]. As demonstrated in Figure 3e, the B 1s spectrum of BiOBr/BNQDs-8.3%, two binding energy peaks at 190.82 and 192.01 eV were detected. These peaks were attributed to the stretching vibrations of the B-N and B-O bonds. As demonstrated in Figure 3f, the peaks observed at 398.1 and 400.72 eV in the N 1s spectrum of BiOBr/BNQDs-8.3% correspond to the B-N and N-O bonds, respectively. In addition, it could be found that the XPS peaks of BiOBr/BNQDs-8.3% presented slight shifts, which was because of the electronic interactions between BiOBr and BNQDs [30].

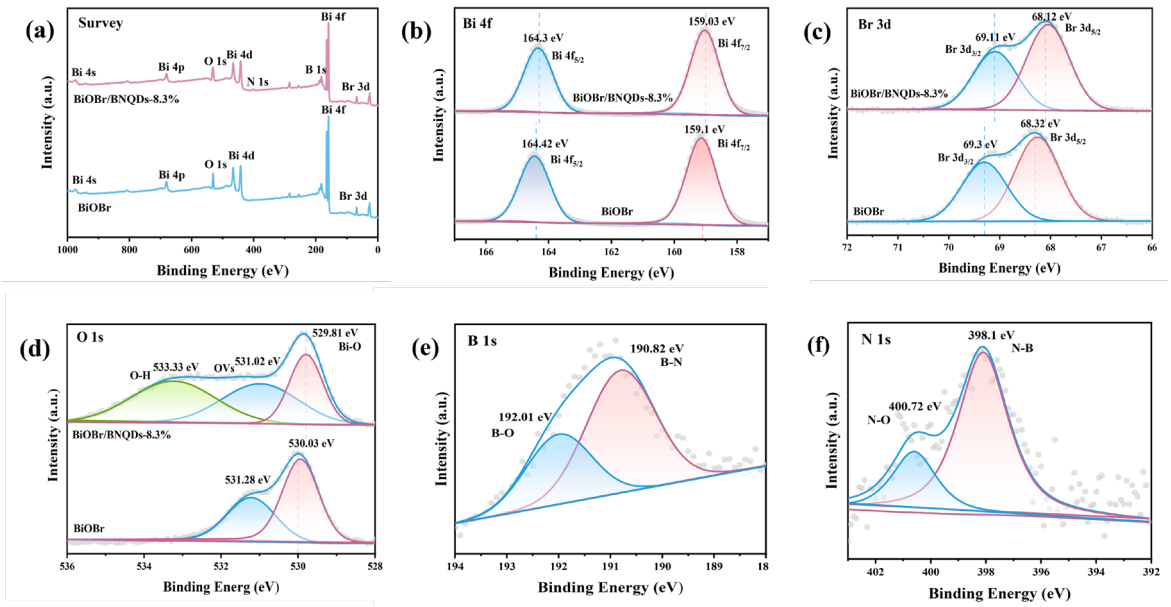

Figure 3. XPS spectra of BiOBr and BiOBr/BNQDs sample: (a) survey, (b) Bi 4f, (c) Br 3d, (d) O 1s, (e) B 1s and (f) N 1s.

The light absorption characteristics of the catalyst samples were studied using UV-Vis diffuse reflection spectroscopy (DRS) within the absorption wavelength range of 200-800 nm. As demonstrated in Figures 4a and S1a, the absorption edge of pure BiOBr is observed at 432 nm. Following the loading of BNQDs, a slight blue shift was observed in the absorption edge. This shift was attributed to the quantum size effect of BNQDs. However, all prepared BiOBr/BNQDs composites exhibited strong absorption characteristics in the wavelength range of $\lambda < 430$ nm [31]. As demonstrated in Figure 4b and Figure S1b, the bandgap values (Eg) of the samples were calculated using Tauc plots and the following equation: $\alpha(hv)=A(hv-Eg)^{n/2}$,where A is constant, α, hv and Eg

 doi:10.20944/preprints202507.1891.v1

refer to the absorption coefficient, photon energy and the bandgap, respectively. In the case of a direct semiconductor, n = 1; conversely, for an indirect semiconductor, n = 4 [32]. As mentioned in previous literature, the n for BiOBr and BNQDs were 4 [33,34]. The estimated bandgaps of BiOBr, BNQDs, BiOBr/BNQDs-2.9%, BiOBr/BNQDs-5.7%, BiOBr/BNQDs-8.3% and BiOBr/BNQDs-10.7% were determined to be 2.56 eV, 4.6 eV, 2.58 eV, 2.59 eV, 2.62 eV and 2.65 eV, respectively. The band structure of the material was determined via Mott-Schottky testing. As shown in Figure 4c-d, the Mott-Schottky curve reveals that the slope of the original BiOBr and BNQDs were positive, the same as n-type semiconductors [35]. The E_{fb} of BiOBr and BNQDs were -1.09 and -0.75 V (vs. Ag/AgCl, PH = 7), respectively. According to $E_{NHE}=E_{Ag/AgCl}$ + 0.197 V, the flat-band potential (E_{fb}) of BiOBr and BNQDs were -0.89 and -0.55 V (vs. NHE, PH = 7), respectively. Then, their conduct band (CB) is more negative by 0.1-0.3 V than E_{fb} for n-type semiconductors [36]; therefore, the conduction band (CB) value of BiOBr and BNQDs were -0.99 and -0.65 V. Employing the formula $E_{VB} = Eg - E_{CB}$, the valence band (VB) value of BiOBr and BNQDs were calculated to be 1.57 and 3.95 eV, respectively.

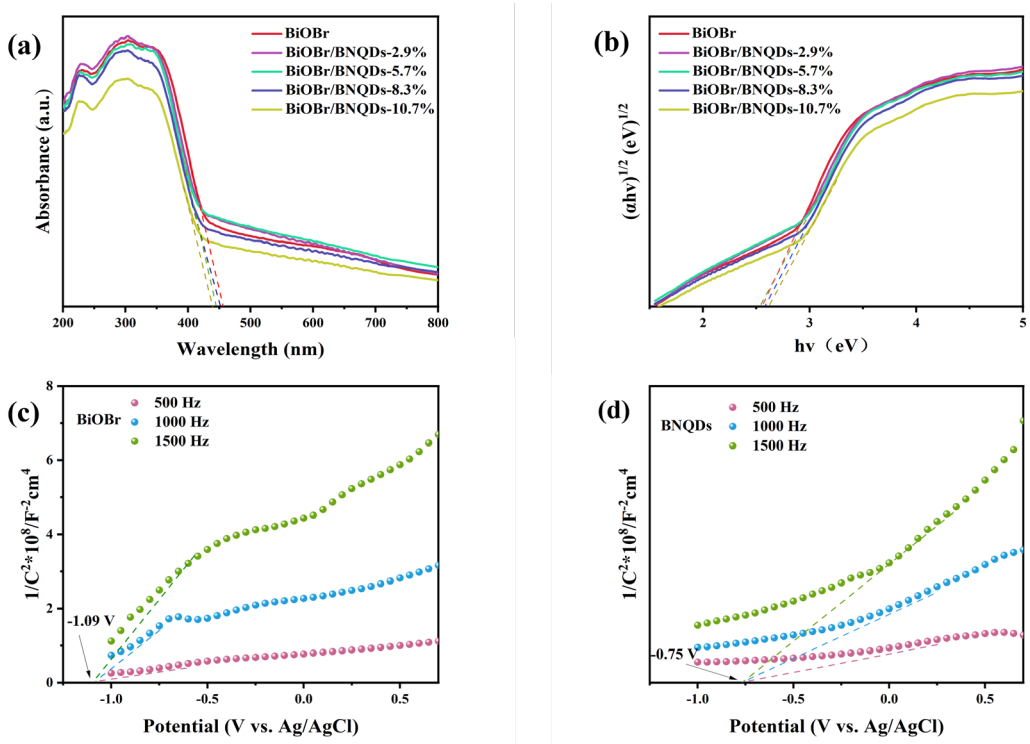

Figure 4. (a) UV-vis spectra, (b) Bandgap Energies, (c) Mott-schottky curves of BiOBr and (d) BNQDs.

The photocatalytic degradation efficiency of the prepared catalyst was evaluated using RhB as the target pollutant in a series of experiments conducted under visible light irradiation. Prior to the photocatalytic degradation experiments, the prepared photocatalyst (30 mg) was first mixed with the prepared RhB solution (20 mg/L) and reacted under dark conditions for 40 min to achieve adsorption-desorption equilibrium. As demonstrated in Figure 5a, the degradation of RhB efficiency of the original BiOBr was only about 78% within 60 min. Nevertheless, following the incorporation of BNQDs, there was a substantial improvement in the overall photocatalytic performance (BiOBr/BNQDs-2.9%: 92%, BiOBr/BNQDs-5.7%: 94.6%, BiOBr/BNQDs-8.3%: 98.56%, BiOBr/BNQDs-10.7%: 96.71%). The outcomes suggested that the effective loading of BNQDs was a pivotal factor in augmenting photocatalytic activity. The photocatalytic degradation process in this experiment could be modeled using a pseudo-first-order kinetic model. As demonstrated in Figure 5b-c, the photocatalytic rate constants (K) of the composite materials were all greater than those of the pure BiOBr photocatalyst [37]. Among all photocatalyst samples, BiOBr/BNQDs-8.3% exhibited the highest degradation rate constant, with a K value of 0.07 min^{-1}, which was 2.8 times greater than the

 doi:10.20944/preprints202507.1891.v1

original BiOBr (0.025 min^{-1}). The enhancement of the photocatalytic degradation activity of the BiOBr/BNQDs composite material toward RhB was attributed to the introduction of BNQDs, which established a rapid charge transfer pathway between BiOBr and BNQDs, thereby effectively reducing the recombination rate of electron-hole pairs. Nevertheless, it was demonstrated that the photocatalytic degradation efficiency of BiOBr was progressively diminished by the excessive loading of BNQDs. This phenomenon was attributed to the excessive addition of BNQDs, which covered the active sites of the original BiOBr, thereby reduced the specific surface area and consequently diminished the light absorption ability [38]. Subsequent electrochemical tests provided further evidence to support this hypothesis.

The cyclic stability of the composite photocatalyst was investigated through a series of cyclic experiments. Following a single photocatalytic degradation of dye, the residual sample in the retained solution was subjected to a centrifugal separation process. The sample was then washed several times with deionized water and anhydrous ethanol, and subsequently dried. The resulting powder was utilized in the subsequent photocatalytic experiment. As demonstrated in Figure 5d, following five cycles of photocatalytic reactions, the degradation rate of RhB by BiOBr/BNQDs-8.3% decreased from 98.56% to 87.58% because of the catalyst lost during the recovery process, yet it still exhibited a satisfactory degradation rate. This finding suggests that the BiOBr/BNQDs-8.3% nanocomposite demonstrates remarkable photocatalytic stability in the degradation of RhB.

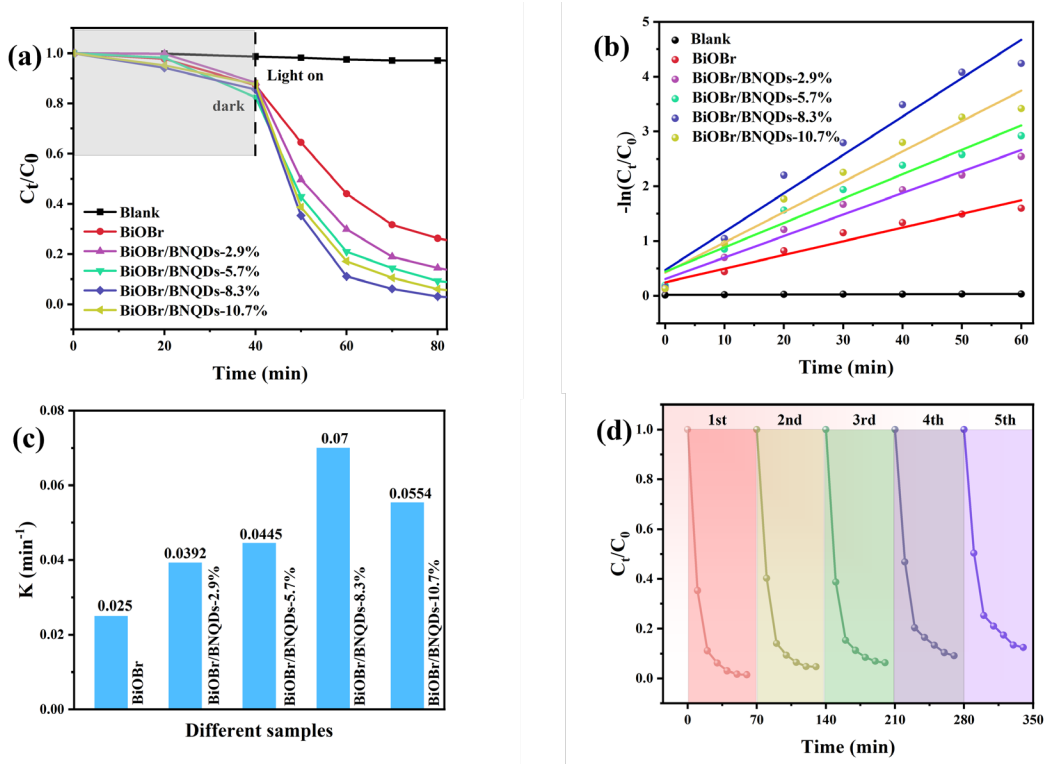

Figure 5. (a) Photocatalytic degradation curves of RhB under visible light irradiation. (b) First-order degradation kinetic curves for the prepared samples and (c) the corresponding degradation rate constants. (d) Results from five-cycle degradation experiments assessing the photocatalytic degradation of RhB using the BiOBr/BNQDs-8.3% photocatalyst.

Electrochemical testing was utilized to assess the charge separation and migration capabilities of the catalyst samples. The PL spectra in Figure 6a were analyzed for the synthesized catalysts at an excitation wavelength of 350 nm. Generally speaking, the lower the fluorescence intensity, the higher the separation efficiency of the electron-hole pair [39]. The primary emission peak center was observed at a wavelength of 470 nm. In comparison to pure BiOBr, all samples containing BNQDs exhibited lower peak intensities. Notably, BiOBr/BNQDs-8.3% demonstrated the lowest peak

 doi:10.20944/preprints202507.1891.v1

intensity, suggesting its optimal charge separation capability [29]. Transient photocurrent response tests (TPR) were conducted on the prepared samples. Conventionally, a more pronounced photocurrent response is indicative of enhanced carrier separation capability [40]. As demonstrated in Figure 6b, all composite samples exhibited an initial peak when illuminated, followed by an increase in peak height. This phenomenon was attributed to the rapid recombination of electron-hole pairs, which resulted in an immediate loss of current. The subsequent gradual rise was due to the ongoing separation of electron-hole pairs, which was driven by the built-in electric field [41]. Among them, BiOBr/BNQDs-8.3% exhibited the highest photocurrent intensity, which was about 3 times that of the original BiOBr. This further indicated that the formation of the heterojunction promoted the rapid migration of electron-hole pairs. The electrochemical impedance spectroscopy (EIS) analysis depicted in Figure 6c demonstrates that BiOBr/BNQDs-8.3% exhibited the smallest arc radius, thereby suggesting that this composite material possessed the lowest charge transfer impedance [42]. The collective outcomes of these experiments suggested the occurrence of efficient migration of charge carriers between the catalysts in the BiOBr/BNQDs-8.3% composite material. The introduction of BNQDs to BiOBr reduced the recombination rate of electron-hole pairs and effectively promoted the photocatalytic degradation of RhB by BiOBr.

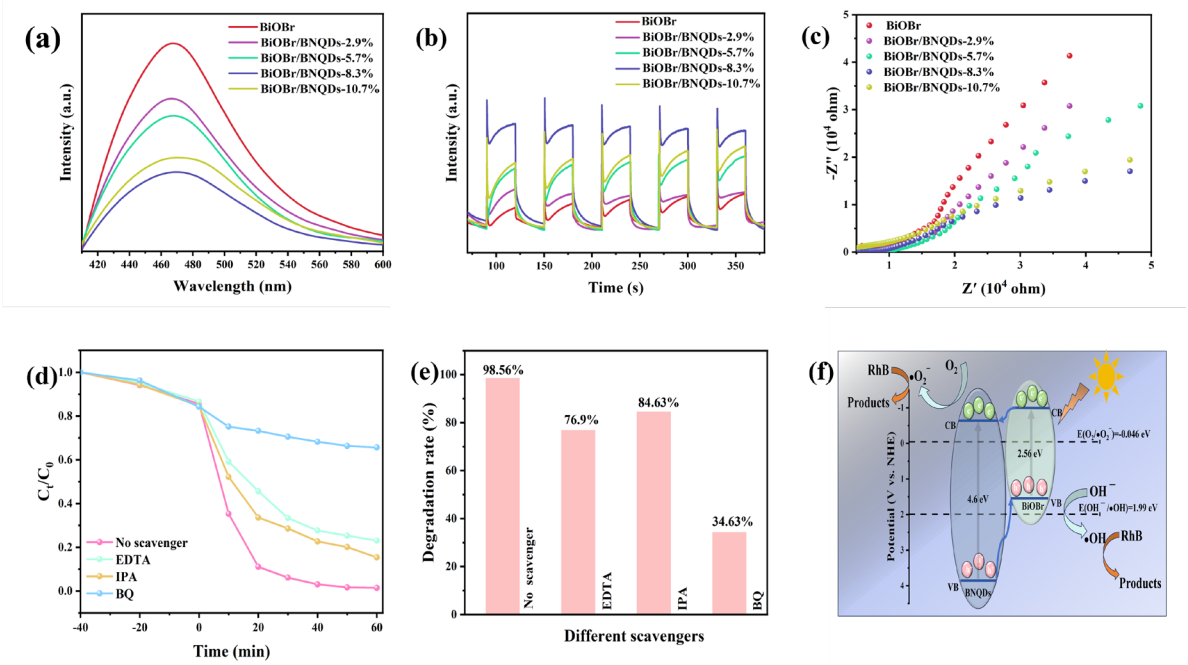

Figure 6. (a) PL spectra, (b) TPR curves and (c) EIS curves for BiOBr and BiOBr/BNQDs with different mass ratios. (d) Degradation curves of BiOBr/BNQDs-8.3% as a photocatalyst after adding different radical scavengers, (e) corresponding degradation rate and (f) Energy band structure diagram of BiOBr and BNQDs.

In order to identify the primary radical species involved in the photocatalytic degradation of RhB, ethylenediaminetetraacetic acid (EDTA), isopropyl alcohol (IPA), and 1,4-benzoquinone (BQ) were selected as quenchers for the hole (h^+), hydroxyl radical (•OH), and superoxide radical ($•O_2^-$) species, respectively [43]. The outcomes of the radical capture experiments were illustrated in Figure 6d-e. In the presence of EDTA and IPA, the degradation efficiency of RhB decreased by 21.66% and 13.93%, respectively. In the presence of BQ, the degradation efficiency of RhB decreased by 63.93%. The experimental findings suggested that $•O_2^-$ were the predominant active radicals responsible for the degradation of RhB, while h^+ and •OH radicals also contributed to the photocatalytic degradation of RhB.

The reaction mechanism of photocatalytic degradation of RhB was analyzed based on the results of radical scavenging experiments and band structure analysis [44–46]. When exposed to visible light,

 doi:10.20944/preprints202507.1891.v1

BiOBr was excited, generating electrons and holes in the conduction and valence bands, respectively. Following the introduction of BNQDs, the synergistic effect of oxygen vacancies and heterojunctions established an efficient electron transport pathway between the BiOBr and BNQDs. The CB position of BiOBr was higher than that of BNQDs, which led to electron transfer to the CB of BNQDs. This process reduced the dissolved oxygen in water to $\bullet O_2^-$ ($E(O_2/\bullet O_2^-)$ = -0.046 eV). Concurrently, the holes present in the VB of BiOBr and those that have accumulated on BNQDs undergo oxidation, resulting in the formation of •OH ($E(OH^-/\bullet OH)$ = 1.99 eV) [47]. Consequently, $\bullet O_2^-$ and •OH (primarily superoxide radicals) were identified as the active oxidative species responsible for RhB degradation in the photocatalytic process. In summary, the loading of BNQDs demonstrated effectively rapid charge transfer on BiOBr nanoflower, thereby facilitating electron transferred to the conduction band of BNQDs. So, the photo-generated holes were concentrated in the VB of BiOBr. The high oxidative ability of $\bullet O_2^-$ further oxidized organic pollutants, thereby achieving efficient degradation of RhB [48].

3. Experimental Section

3.1. Materials

Pentahydrate bismuth nitrate ($Bi(NO_3)_3{\cdot}5H_2O$), hexadecyl trimethyl ammonium bromide (CTAB), boric acid (H_3BO_3), melamine ($C_3H_6N_6$), ethylene glycol (Eg), and isopropyl alcohol (IPA) were brought from Aladdin (Shanghai, China). Absolute ethanol and Rhodamine B (RhB) were brought from Titan (Shanghai, China). All reagents used in this study were analytical grade and did not require further purification.

3.2. Preparation of Photocatalysts

3.2.1. Synthesis of BiOBr

Dissolved 8 mmol of CTAB and 8 mmol of Bi $(NO_3)_3{\cdot}5H_2O$ in 36 mL of Eg. The solution was stirred for 30 min, then 24 mL of IPA was slowly added, and stirred again for 1 h. The solution was transferred to a 100 mL high-pressure reactor lined with polytetrafluoroethylene. The autoclave was then placed in an oven and the temperature was increased to 160℃, where it remained for a total of 12 h. The product was cooled to room temperature, washed multiple times with ultra-pure water and anhydrous ethanol, and then dried in a vacuum oven at 60°C for 12 h [22,49].

3.2.2. Synthesis of BNQDs

Dissolved 4.8 mmol of boric acid and 2.4 mmol of melamine completely in 30 mL of ultrapure water, then transferred the mixture to a 100 mL high-pressure reactor lined with polytetrafluoroethylene (PTFE). Reacted at 200°C in a muffle furnace for 15 h. The obtained product was BNQDs solution (1.8 g/L) [50].

3.2.3. Synthesis of BiOBr/BNQDs-X%

BNQDs solutions (0.5, 1, 1.5, and 2 mL) were added into 10 mL of ethanol with 30 mg BiOBr powder separately, stirred at room temperature for 1 h. The samples were centrifugal separated then dried in a vacuum oven for 6 h. The samples with different amounts of BNQDs added were named BNQDs-X, where X represents the mass ratio of BNQDs added. These materials were respectively named BiOBr/BNQDs-2.9%, BiOBr/BNQDs-5.7%, BiOBr/BNQDs-8.3%, and BiOBr/BNQDs-10.7% [51].

3.3. Photocatalytic Activity Experiment

This experiment evaluated the photocatalytic performance of the sample by measuring its efficiency in degrading RhB under visible light irradiation. Degradation experiments were conducted using a photochemical reaction instrument (BL-GHX-V, Shanghai Bilang Instrument Manufacturing

 doi:10.20944/preprints202507.1891.v1

Co., Ltd., Shanghai, China). The experiment used a 300 W xenon lamp as the visible light source. First, 30 mg of BiOBr/BNQDs photocatalyst was dispersed in 50 mL of RhB solution (20 mg/L), stirred for 40 min in the dark condition to achieve adsorption-desorption equilibrium. The suspension was then exposed to visible light for photocatalytic degradation for 60 min. Every 10 min, 4.0 mL of the suspension was collected and centrifuged. The absorbance of the supernatant after centrifugation was measured using a UV-1860 spectrophotometer (UNICO, Shanghai China) at the maximum wavelength of 550 nm [48].

3.4. Characterizations

X-ray diffraction (XRD) analysis was conducted by measuring the X-ray scattering angle and intensity to determine the crystal structure of the sample. Fourier transformed infrared (FT-IR) spectroscopy (Nicolet IS6050, Waltham, MA, USA) was employed to investigate infrared spectra within the 4000–400 cm^{-1} range. The microstructure was observed using a scanning electron microscope (SEM, ZEISS Gemini 300) and high-resolution TEM (Regulus8230). X-ray photoelectron spectroscopy (XPS) analysis was utilized for characterizing the chemical states of constituent elements. The analysis of the light absorption characteristics of the catalyst was conducted by employing a UV-visible absorption spectrometer (UV3600PLUS). A steady state/transient fluorescence spectrometer (PL, QM/TM) with an excitation wavelength of 380 nm was used to measure the fluorescence intensity of the material.

3.5. Photoelectrochemical Property

Photoelectrochemical tests were conducted using the CHI660 workstation (Shanghai Chenhua, CHI 660F) with a 0.5 M sodium sulfate solution. The working electrode was composed of Pt nanosheets, while Ag/AgCl was utilized as the reference electrode. The working electrode was prepared using a drop-coating process. Initially, 5 mg of the BiOBr/BNQDs sample was placed into a sample tube, followed by the sequential addition of 25 μL of naphthol and 475 μL of ethanol. Subsequently, the drop-coating solution was applied to a sterile 1 cm × 1 cm FTO glass substrate and dried at room temperature for 12 h to ensure complete solidification of the sample. Transient photocurrent response (TPR) was tested using a 300 W xenon arc lamp. Electrical impedance spectroscopy (EIS) measurements were conducted at a voltage of 1.0 V relative to the reversible hydrogen electrode (RHE), with a perturbation amplitude of 10 mV under open-circuit voltage conditions. These measurements span a frequency range from 0.1 MHz to 0.01 Hz. Mott-Schottky curves were also measured at 500, 1000, and 1500 Hz while the system was in dark condition.

4. Conclusions

In conclusion, a novel BiOBr/BNQDs heterostructure catalyst was constructed by integrating, nanoflower-like BiOBr microspheres with zero-dimensional BNQDs. The resulting composite exhibited a large specific surface area and abundant active sites, which facilitated the rapid and efficient degradation of RhB under visible light. The introduction of BNQDs not only promoted charge separation but also significantly enhanced the redox capacity of the photocatalytic system. Among the synthesized materials, the BiOBr/BNQDs-8.3% composite demonstrated the highest activity, achieving a degradation efficiency of 98.56% within 60 min and maintaining excellent stability over five consecutive cycles. Mechanism investigations based on radical scavenging experiments and band structure analysis confirmed the synergistic effect between BiOBr and BNQDs. This study provides valuable insights into the rational design of high-performance heterostructure photocatalysts for environmental remediation.

Supplementary Materials: The following supporting information can be downloaded at the website of this paper posted on Preprints.org, Figure S1. UV-vis DRS spectra and Band gap values of BNQDs samples by using the Kubelka-Munk model. Table S1. Slopes and R^2 of catalysts.

 doi:10.20944/preprints202507.1891.v1

Author Contributions: Conceptualization, Y.Q.; methodology, Y.Q. and T.W.; software, Y.Q.; validation, Y.Q. and X.P.; formal analysis, Y.Q.; investigation, Y.Q. X.P. and T.W.; resources, Y.Q.; data curation, Y.Q.; writing-original draft preparation, Y.Q.; writing-review and editing, L.Z.; visualization, Y.Q.; supervision, Y.Z., H.X., L.Z. and Z.M.; project administration, L.Z. and Z.M.; funding acquisition, L.Z. and Z.M. All authors have read and agreed to the published version of the manuscript.

Funding: This work was supported by National Natural Science Foundation of China (21872025).

Data Availability Statement: The raw data supporting the conclusions of this article will be made available by the authors on request.

Conflicts of Interest: The authors declare no conflicts of interest.

References

1. Uddin, F. Environmental hazard in textile dyeing wastewater from local textile industry. *Cellulose*. **2021**, 28(17), p. 10715-10739.
2. Liu, H.;Zhang, J.;Lu, M.;Liang, L.;Zhang, H..Wei, J. Biosynthesis based membrane filtration coupled with iron nanoparticles reduction process in removal of dyes. *Chemical Engineering Journal*. **2020**, 387.
3. Pitcheri, R.;Mooni, S.P.;Harikrishnan, L.;Raghav, J.;Roy, S.;Maaouni, N.;Radhalayam, D.;Alothman, A.A.;Alharbi, A.F.;Al-Zahrani, F.A.M.;Nunna, G.P..Ko, T.J. Novel S-scheme β-$Cu_2V_2O_7$/Ni/Pg-C_3N_4 heterojunction photocatalyst for sunlight-induced degradation of RhB. *Surfaces and Interfaces*. **2024**, 52.
4. Basely, A.M.;Shaker, M.H.;Helmy, F.M.;Abdel-Messih, M.F..Ahmed, M.A. Construction of Bi_2S_3/g-C_3N_4 step S-scheme heterojunctions for photothermal decomposition of rhodamine B dye under natural sunlight radiations. *Inorganic Chemistry Communications*. **2023**, 148.
5. Liang, H.;Zhao, J.;Brouzgou, A.;Wang, A.;Jing, S.;Kannan, P.;Chen, F..Tsiakaras, P. Efficient photocatalytic H_2O_2 production and photodegradation of RhB over K-doped g-C_3N_4/ZnO S-scheme heterojunction. *Journal of Colloid and Interface Science*. **2025**, 677, p. 1120-1133.
6. Liu, Y.;Hu, Z..Yu, J.C. Photocatalytic degradation of ibuprofen on S-doped BiOBr. *Chemosphere*. **2021**, 278.
7. Huang, S.;Wang, Y.;Wan, J.;Yan, Z.;Ma, Y.;Zhang, G..Wang, S. Ti_3C_2Tx as electron-hole transfer mediators to enhance AgBr/BiOBr Z heterojunction photocatalytic for the degradation of Tetrabromobisphenol A: Mechanism Insight. *Applied Catalysis B: Environmental*. **2022**, 319.
8. Wang, C.;Wang, J..Yu, X. Enhancement of photocatalytic ammonia production over BiOBr nanosheets with photo-assembled Au cocatalysts. *Colloids and Surfaces A: Physicochemical and Engineering Aspects*. **2023**, 662.
9. Xia, Y.;Xia, X.;Chen, L.;Liang, R.;Yan, G..Liang, S. O defect anchored Ru on BiOBr with nanoconfined structure for catalytic N_2 fixation. *Applied Catalysis B: Environment and Energy*. **2024**, 349.
10. Sun, J.;Zhang, Y.;Fan, S.;Li, X..Zhao, Q. An efficient Z-type CeO_2/BiOBr heterostructure with enhanced photo-oxidation degradation of o-DCB and CO_2 reduction ability. *Applied Catalysis B: Environment and Energy*. **2024**, 356.
11. Zhang, K.;Zhang, Y.;Zhang, D.;Liu, C.;Zhou, X.;Yang, H.;Qu, J..He, D. Efficient photocatalytic water disinfection by a novel BP/BiOBr S-scheme heterojunction photocatalyst. *Chemical Engineering Journal*. **2023**, 468.
12. Cao, T.;Xu, Q.;Zhang, J.;Wang, S.;Di, T..Deng, Q. S-scheme g-C_3N_4/BiOBr heterojunction for efficient photocatalytic H_2O_2 production. *Chinese Journal of Catalysis*. **2025**, 72, p. 118-129.
13. Yu, Y.;Zhang, P.;Tuerhong, R.;Chai, K.;Du, X.;Su, X.;Zhao, L..Han, L. Regulating the electronic structure of BiOBr by Cu-doping to promote efficient photocatalytic nitrogen fixation reaction. *Separation and Purification Technology*. **2025**, 364.
14. Liu, J.;Qin, W.;Wang, Y.;Xu, Q.;Xie, Y.;Chen, Y.;Dai, Y..Zhang, W. NH_2-UiO-66 modification BiOBr enhancement photoreduction CO_2 to CO. *Separation and Purification Technology*. **2024**, 344.
15. Ning, J.;Zhang, B.;Siqin, L.;Liu, G.;Wu, Q.;Xue, S.;Shao, T.;Zhang, F.;Zhang, W..Liu, X. Designing advanced S-scheme CdS QDs/La-Bi_2WO_6 photocatalysts for efficient degradation of RhB. *Exploration*. **2023**, 3(5).
16. Li, S.;Yang, Y.;Niu, J.;Zheng, H.;Zhang, W.;Leong, Y.K.;Chang, J.-S..Lai, B. Activation of PAA at the Fe–Nx Sites by Boron Nitride Quantum Dots Enhanced Charge Transfer Generates High-Valent Metal-Oxo Species for Antibiotics Degradation. *Environmental Science & Technology*. **2024**, 58(49), p. 21871-21881.

 doi:10.20944/preprints202507.1891.v1

17. Dong, H.;Yin, B.;Li, J.;Guo, W.;Meng, D.;Zhu, X.;Zhang, G.;Zhang, G.;Xin, Y..Chen, Q. Photocatalytic remediation of fluoranthene contaminated soil by eco-friendly GQDs/TiO_2/α-FeOOH composite photocatalyst: Efficiency, influence factors, mechanism, and toxicity analysis. *Separation and Purification Technology*. **2025**, 357.
18. Cheng, M.;Li, H.;Wu, Z.;Yu, Z.;Tao, X..Huang, L. Synergistic effects of CQDs and oxygen vacancies on CeO_2 photocatalyst for efficient photocatalytic nitrogen fixation. *Separation and Purification Technology*. **2025**, 354.
19. Su, X.;Dong, Y.;Zhu, Y..Shi, H. MIL-125-NH_2/BNQDs persistent photocatalyst enhanced peroxymonosulfate activation for efficient PET plastics removal. *Chemical Engineering Journal*. **2024**, 501.
20. Guo, J.;Hou, J.;Yang, Z.;Xia, J.;Wu, J.;You, G..Miao, L. Boron nitride quantum dots supported hollow NH_2-MIL-125 drive photo-Fenton-PMS system for photocatalytic tetracycline degradation: Contribution of tannic acid etching. *Chemosphere*. **2024**, 365.
21. Zhang, Q.;Peng, Y.;Lin, Y.;Wu, S.;Yu, X..Yang, C. Bisphenol S-doped g-C_3N_4 nanosheets modified by boron nitride quantum dots as efficient visible-light-driven photocatalysts for degradation of sulfamethazine. *Chemical Engineering Journal*. **2021**, 405.
22. Wu, J.;Xie, Y.;Ling, Y.;Si, J.;Li, X.;Wang, J.;Ye, H.;Zhao, J.;Li, S.;Zhao, Q..Hou, Y. One-step synthesis and Gd^{3+} decoration of BiOBr microspheres consisting of nanosheets toward improving photocatalytic reduction of CO_2 into hydrocarbon fuel. *Chemical Engineering Journal*. **2020**, 400.
23. Chen, R.;Zhang, H.;Dong, Y..Shi, H. Dual metal ions/BNQDs boost PMS activation over copper tungstate photocatalyst for antibiotic removal: Intermediate, toxicity assessment and mechanism. *Journal of Materials Science & Technology*. **2024**, 170, p. 11-24.
24. Ren, K.;Zhao, W.;Zhai, Z.;Han, T..Shi, H. 2D/0D Bi_2MoO_6 nanosheets/BN quantum dots photocatalysts with enhanced charge separation for efficient elimination of antibiotic. *Applied Surface Science*. **2021**, 562.
25. Sun, J.;Li, X.;Zhao, Q..Liu, B. Ultrathin nanoflake-assembled hierarchical BiOBr microflower with highly exposed {001} facets for efficient photocatalytic degradation of gaseous ortho-dichlorobenzene. *Applied Catalysis B: Environmental*. **2021**, 281.
26. Ren, K.;Lv, M.;Xie, Q.;Zhang, C..Shi, H. Dual BN quantum dot/Ag co-catalysts synergistically promote electron-hole separation on g-C_3N_4 nanosheets for efficient antibiotics oxidation and Cr(VI) reduction. *Carbon*. **2022**, 186, p. 355-366.
27. Miao, Z.;Zhang, Y.;Wang, N.;Xu, P..Wang, X. BiOBr/Bi_2S_3 heterojunction with S-scheme structureand oxygen defects: In-situ construction and photocatalytic behavior for reduction of CO_2 with H_2O. *Journal of Colloid and Interface Science*. **2022**, 620, p. 407-418.
28. Wang, Y.;Wang, K.;Wang, J.;Wu, X..Zhang, G. Sb_2WO_6/BiOBr 2D nanocomposite S-scheme photocatalyst for NO removal. *Journal of Materials Science & Technology*. **2020**, 56, p. 236-243.
29. Cheng, T.;Xing, Z.;Zhang, N.;Sun, P.;Peng, H.;Li, Z.;Wang, N..Zhou, W. Ti_3C_2 quantum dots-modified oxygen-vacancy-rich BiOBr hollow microspheres toward optimized photocatalytic performance. *Chemosphere*. **2024**, 364.
30. Fu, S.;Yuan, W.;Liu, X.;Yan, Y.;Liu, H.;Li, L.;Zhao, F..Zhou, J. A novel 0D/2D WS_2/BiOBr heterostructure with rich oxygen vacancies for enhanced broad-spectrum photocatalytic performance. *Journal of Colloid and Interface Science*. **2020**, 569, p. 150-163.
31. Wang, Z.;Wang, K.;Li, Y.;Jiang, L..Zhang, G. Novel $BiSbO_4$/BiOBr nanoarchitecture with enhanced visible-light driven photocatalytic performance: Oxygen-induced pathway of activation and mechanism unveiling. *Applied Surface Science*. **2019**, 498.
32. Liu, H.;Wang, B.;Chen, M.;Zhang, H.;Peng, J.;Ding, L..Wang, W. Simple synthesis of BiOAc/BiOBr heterojunction composites for the efficient photocatalytic removal of organic pollutants. *Separation and Purification Technology*. **2021**, 261.
33. Chen, X.;Wu, Y.;Tang, Y.;Li, P.;Gao, S.;Wang, Q.;Liu, W..Zhan, S. Construction of Z-scheme Cu-CeO_2/BiOBr heterojunction for enhanced photocatalytic degradation of sulfathiazole. *Chinese Chemical Letters*. **2024**, 35(7).
34. Ren, K.;Dong, Y.;Chen, Y..Shi, H. Bi_2WO_6 nanosheets assembled BN quantum dots: Enhanced charge separation and photocatalytic antibiotics degradation. *Colloids and Surfaces A: Physicochemical and Engineering Aspects*. **2022**, 637.

 doi:10.20944/preprints202507.1891.v1

35. Chen, L.;Li, H.;Li, H.;Li, H.;Qi, W.;Zhang, Q.;Zhu, J.;Zhao, P..Yang, S. Accelerating photogenerated charge kinetics via the g-C_3N_4 Schottky junction for enhanced visible-light-driven CO_2 reduction. *Applied Catalysis B: Environmental*. **2022**, 318.
36. Xu, J.;Wang, Y.;Niu, J..Chen, M. Facile construction of BiOBr/BiOCOOH p-n heterojunction photocatalysts with improved visible-light-driven photocatalytic performance. *Separation and Purification Technology*. **2019**, 225, p. 24-32.
37. Liu, C.;Mao, S.;Shi, M.;Hong, X.;Wang, D.;Wang, F.;Xia, M..Chen, Q. Enhanced photocatalytic degradation performance of $BiVO_4$/BiOBr through combining Fermi level alteration and oxygen defect engineering. *Chemical Engineering Journal*. **2022**, 449.
38. Xu, H.;Yang, J.;Li, Y.;Fu, F.;Da, K.;Cao, S.;Chen, W..Fan, X. Fabrication of Bi_2O_3 QDs decorated TiO_2/BiOBr dual Z-scheme photocatalysts for efficient degradation of gaseous toluene under visible-light. *Journal of Alloys and Compounds*. **2023**, 950.
39. Tang, Q.-Y.;Yang, M.-J.;Yang, S.-Y..Xu, Y.-H. Enhanced photocatalytic degradation of glyphosate over 2D CoS/BiOBr heterojunctions under visible light irradiation. *Journal of Hazardous Materials*. **2021**, 407.
40. Gao, X.;Shan, P.;Shi, W..Guo, F. Photothermal-Assisted Photocatalytic Degradation of Antibiotic by Black g-C_3N_4 Materials Derived from C/N Precursors and Tetrachlorofluorescein. *Catalysts*. **2025**, 15(5).
41. Li, Z.;Wang, P.;Ren, C.;Wu, L.;Yao, Y.;Zhong, S.;Lin, H.;Zhao, L.;Gao, Y..Bai, S. Modulating the Selectivity of CO_2 Photoreduction by Regulating the Location of PtCu in a UiO-66@$ZnIn_2S_4$ Core–Shell Nanoreactor. *ACS Catalysis*. **2024**, 15(2), p. 828-840.
42. Li, S.;Zeng, H.;Fan, J.;Zhu, M.;Zhang, C.;An, X.;Luo, Z.;Fu, H..Yang, X. Incorporating Ag Nanocrystals with $LaFeO_3$ Photocathodes Towards Greatly Enhanced Photoelectrocatalytic Properties. *Catalysts*. **2025**, 15(5).
43. Zhao, W.;Wang, W.;Han, T.;Wang, H.;Zhang, H..Shi, H. Oxygen vacancies boosted charge separation towards enhanced photodegradation ability over 3D/2D Z-scheme BiO_1–XBr/Fe_2O_3 heterostructures. *Separation and Purification Technology*. **2021**, 269.
44. Zhang, P.;Wang, Z.;Zhao, L.;Li, L.;Li, N.;Su, X..Su, Q. Construction of a novel 0D-3D boron nitride quantum dots /NH_2-MIL-125(Ti) composite for photodegradation of Rhodamine B. *Materials Science in Semiconductor Processing*. **2023**, 167.
45. Ni, Q.;Ke, X.;Qian, W.;Yan, Z.;Luan, J..Liu, W. Insight into tetracycline photocatalytic degradation mechanism in a wide pH range on BiOI/BiOBr: Coupling DFT/QSAR simulations with experiments. *Applied Catalysis B: Environmental*. **2024**, 340.
46. Long, Z.;Zhang, G.;Du, H.;Zhu, J..Li, J. Preparation and application of BiOBr-Bi_2S_3 heterojunctions for efficient photocatalytic removal of Cr(VI). *Journal of Hazardous Materials*. **2021**, 407.
47. Kanagaraj, T..Thiripuranthagan, S. Photocatalytic activities of novel $SrTiO_3$—BiOBr heterojunction catalysts towards the degradation of reactive dyes. *Applied Catalysis B: Environmental*. **2017**, 207, p. 218-232.
48. Zhong, R.;Liao, H.;Deng, Q.;Zou, X..Wu, L. Preparation of a novel composite photocatalyst BiOBr/ZIF-67 for enhanced visible-light photocatalytic degradation of RhB. *Journal of Molecular Structure*. **2022**, 1259.
49. Jiao, W.;Xie, Y.;He, F.;Wang, K.;Ling, Y.;Hu, Y.;Wang, J.;Ye, H.;Wu, J..Hou, Y. A visible light-response flower-like La-doped BiOBr nanosheets with enhanced performance for photoreducing CO_2 to CH_3OH. *Chemical Engineering Journal*. **2021**, 418.
50. Liu, T.;Liu, J.;Yang, Y.;Wang, X.;Zhou, T.;Yin, G.;Jia, F..Liu, B. 1D 2D and 3D anatase TiO_2 sensitized with BNQDs for sensitive acetone detection. *Surfaces and Interfaces*. **2023**, 38.
51. Huang, H.;Chen, Y..Shi, H. Boosting Separation of Charge Carriers in 2D/0D BiOBr Nanoflower Sheets/BN Quantum Dots with the Lorentz Force via Magnetic Field. *Energy & Fuels*. **2022**, 36(19), p. 11495-11502.